Intracranial Calcifications and Hemorrhages: Characterization with Quantitative Susceptibility Mapping[1]

Weiwei Chen, MD, PhD
Wenzhen Zhu, MD
Ilhami Kovanlikaya, MD
Arzu Kovanlikaya, MD
Tian Liu, PhD
Shuai Wang, MS
Carlo Salustri, PhD
Yi Wang, PhD

Purpose: To compare gradient-echo (GRE) phase magnetic resonance (MR) imaging and quantitative susceptibility mapping (QSM) in the detection of intracranial calcifications and hemorrhages.

Materials and Methods: This retrospective study was approved by the institutional review board. Thirty-eight patients (24 male, 14 female; mean age, 33 years ± 16 [standard deviation]) with intracranial calcifications and/or hemorrhages diagnosed on the basis of computed tomography (CT), MR imaging (interval between examinations, 1.78 days ± 1.31), and clinical information were selected. GRE and QSM images were reconstructed from the same GRE data. Two experienced neuroradiologists independently identified the calcifications and hemorrhages on the QSM and GRE phase images in two randomized sessions. Sensitivity, specificity, and interobserver agreement were computed and compared with the McNemar test and κ coefficients. Calcification loads and volumes were measured to gauge intermodality correlations with CT.

Results: A total of 156 lesions were detected: 62 hemorrhages, 89 calcifications, and five mixed lesions containing both hemorrhage and calcification. Most of these lesions (146 of 151 lesions, 96.7%) had a dominant sign on QSM images suggestive of a specific diagnosis of hemorrhage or calcium, whereas half of these lesions (76 of 151, 50.3%) were heterogeneous on GRE phase images and thus were difficult to characterize. Averaged over the two independent observers for detecting hemorrhages, QSM achieved a sensitivity of 89.5% and a specificity of 94.5%, which were significantly higher than those at GRE phase imaging (71% and 80%, respectively; $P < .05$ for both readers). In the identification of calcifications, QSM achieved a sensitivity of 80.5%, which was marginally higher than that with GRE phase imaging (71%; $P = .08$ and .10 for the two readers), and a specificity of 93.5%, which was significantly higher than that with GRE phase imaging (76.5%; $P < .05$ for both readers). QSM achieved significantly better interobserver agreements than GRE phase imaging in the differentiation of hemorrhage from calcification (κ: 0.91 vs 0.55, respectively; $P < .05$).

Conclusion: QSM is superior to GRE phase imaging in the differentiation of intracranial calcifications from hemorrhages and with regard to the sensitivity and specificity of detecting hemorrhages and the specificity of detecting calcifications.

Online supplemental material is available for this article.

[1] From the Department of Radiology, Tongji Hospital, Tongji Medical College, Huazhong University of Science & Technology, Wuhan, China (W.C., W.Z.); Department of Radiology, Weill Cornell Medical College, 515 E 71st St, New York, NY 10021 (W.C., I.K., A.K., T.L., S.W., C.S., Y.W.); Department of Biomedical Engineering, Cornell University, Ithaca, NY (Y.W.); Department of Biomedical Engineering, Kyung Hee University, Seoul, South Korea (Y.W.); School of Electronic Engineering, University of Electronic Science and Technology of China, Chengdu, China (S.W.); and Institute of Cognitive Sciences and Technologies, Fatebenefratelli Hospital, Rome, Italy (C.S.). Received January 11, 2013; revision requested April 28; revision received June 29; accepted July 16; final version accepted August 12. Supported by the Doctoral Fund of Ministry of Education of China (grant 200804871039). **Address correspondence to** Y.W. (e-mail: *yiwang@med.cornell.edu*).

Hemorrhage and calcification are common pathologic components of many intracranial diseases. Reliable differentiation between hemorrhages and calcifications is crucial for accurate diagnosis, prognosis, and therapy optimization. For example, the presence of a hemorrhage may suggest a possible stroke, traumatic brain injury, or a malignant tumor, whereas the presence of calcifications is suggestive of different diseases, such as Sturge-Weber syndrome, tuberous sclerosis, neurocysticercosis, or craniopharyngiomas (1,2). The differentiation of intracranial microbleeds from multiple calcified cysticercus granulomas is essential for choosing an appropriate treatment for patients affected by both neurocysticercosis and hypertension (3).

Currently, magnetic resonance (MR) imaging and computed tomography (CT) are considered complementary in the detection of hemorrhages and calcifications. In particular, gradient-echo (GRE) MR imaging is as accurate as CT in the detection of acute hemorrhages and more accurate than CT in the detection of chronic hemorrhages (4); however, calcifications may be mistaken for chronic hemorrhage on GRE magnitude images because both appear hypointense. Unfortunately, calcifications also generate nonspecific signal intensities on conventional T1- and T2-weighted spin-echo images (5). For these reasons, CT is preferred in the detection of calcifications and is widely used in clinical practice despite its use of ionizing radiation (6).

Recent advances have suggested that MR imaging may help differentiate calcifications from hemorrhages on the basis of their tissue magnetic susceptibilities. Although calcifications are diamagnetic relative to brain parenchyma, most blood-related products, such as deoxyhemoglobin and hemosiderin, are paramagnetic (7). GRE phase imaging has been used as a tool for differentiating between diamagnetic and paramagnetic substances (3,8–11). However, field inhomogeneity is a convolution of, not equal to, the local tissue susceptibility property. The appearance of calcifications and hemorrhages on GRE phase images is dependent on field strength, echo time, tissue orientation relative to the main magnetic field, and the plane of observation (9,12–14). Deconvolution of the field inhomogeneity is necessary for quantitative mapping of magnetic susceptibility. Recently, quantitative susceptibility mapping (QSM) has been established (13,15,16) and has been suggested for differentiating diamagnetic calcifications from paramagnetic hemorrhages (9,17,18).

We performed this study to compare GRE phase imaging and QSM in the detection of intracranial calcifications and hemorrhages.

Advances in Knowledge

- The large majority of lesions containing calcification or hemorrhage (146 of 151 lesions, 96.7%) showed interpretable findings at quantitative susceptibility mapping (QSM); approximately half of these lesions (76 of 151 lesions, 50.3%) appeared difficult to interpret on gradient-echo (GRE) phase images.
- Compared with GRE phase imaging, QSM provided better sensitivity (71% vs 89.5%, respectively) and specificity (80% vs 94.5%, respectively) in the detection of hemorrhages ($P < .05$); QSM provided more specific detection of calcification than GRE phase imaging (93.5% vs 76.5%, $P < .05$) and better interobserver agreements in the differentiation of calcifications from hemorrhagic lesions (κ: 0.91 vs 0.55, $P < .05$).
- At QSM, lesions with calcification appeared diamagnetic when they were outside deep brain nuclei and either diamagnetic or paramagnetic when they were in deep brain nuclei.
- QSM provided accurate measurements of volume and total susceptibility of calcification lesions referencing to CT.

Implication for Patient Care

- QSM may enable differentiation of intracranial calcifications from hemorrhages at MR imaging.

Materials and Methods

Patients

Between March and August 2010, 67 consecutive patients without acute hemorrhage who underwent both CT and MR imaging examinations within 1 week at our institution were retrospectively enrolled in this institutional review board–approved study. Twenty-nine patients were excluded owing to lack of pathologic intracranial calcifications or hemorrhages ($n = 24$), poor image quality owing to movement ($n = 3$), and incomplete data in the picture archiving and communication system ($n = 2$). Thus, a subset of 38 patients (24 male and 14 female patients aged 6–75 years [mean age ± standard deviation, 33 years ± 16]) with intracranial pathologic calcifications or nonacute hemorrhages (including late subacute and chronic hemorrhages

Published online before print
10.1148/radiol.13122640 **Content code:** NR

Radiology 2014; 270:496–505

Abbreviations:
GRE = gradient echo
QSM = quantitative susceptibility mapping

Author contributions:
Guarantors of integrity of entire study, W.C., Y.W.; study concepts/study design or data acquisition or data analysis/interpretation, all authors; manuscript drafting or manuscript revision for important intellectual content, all authors; manuscript final version approval, all authors; literature research, W.C., W.Z., T.L., S.W., C.S., Y.W.; clinical studies, W.C., W.Z., I.K., A.K., Y.W.; statistical analysis, W.C., W.Z., T.L., S.W., C.S., Y.W.; and manuscript editing, W.C., W.Z., I.K., A.K., T.L., C.S., Y.W.

Funding:
This research was supported by the National Institutes of Health (grant R01EB013443-01).

Conflicts of interest are listed at the end of this article.

Table 1

Criteria for the Identification of Calcified and/or Hemorrhagic Lesions

Category	Criteria
Calcified lesion	Hyperattenuation (≥100 HU) at CT; hyperattenuation (<100 HU) at CT and pathologic proof
Nonacute hemorrhagic lesion (including microbleed)	Late subacute and chronic hemorrhages: iso- and/or hypoattenuation at CT and typical appearance at MR imaging (T1-weighted, T2-weighted, and T2*-weighted imaging) as described by Huisman (1) and medical history of hemorrhagic stroke; microbleeds: invisible at CT and hypointense on T2*-weighted magnitude images and medical history with diseases prone to bleeding (eg, hypertension, diabetes) but without diseases related to calcium deposits (eg, neurocysticercosis, tuberculosis)
Calcified and hemorrhagic lesion	Calcified and hemorrhagic lesions (regions) interconnected into a single lesion

and microbleeds) were selected. The interval between CT and MR imaging ranged from 0.5 to 5 days (mean, 1.78 days ± 1.31). The underlying diseases were as follows: vascular malformation (n = 14), intracranial neoplasm (n = 7), neurocysticercosis (n = 6), tuberous sclerosis (n = 1), chronic hemorrhages (n = 2), Fahr disease (n = 1), hypoparathyroidism with trauma (n = 1), Sturge-Weber syndrome (n = 1), trauma (n = 2), tuberculosis (n = 3), and schistosome (n = 2).

Imaging Protocol and Data Reconstruction

MR imaging was performed with a 3.0-T MR system (Signa HDxt; GE Healthcare, Waukesha, Wis) by using an eight-channel head coil and the following pulse sequences for each patient: *(a)* T1-weighted spin echo, *(b)* T2-weighted fast spin echo, *(c)* T2-weighted fluid-attenuated inversion recovery, and *(d)* T2*-weighted spoiled multiecho GRE. Imaging parameters for the multiecho GRE sequence were as follows: flip angle, 20°; repetition time, 57 msec; number of echoes, eight; first echo time, 5.7 msec; echo time spacing, 6.7 msec; bandwidth, 41.67 kHz; field of view, 24 cm; matrix, 416 × 320; section thickness, 2 mm; parallel imaging acceleration factor, 2; and total acquisition time, 6 minutes 12 seconds.

QSM and GRE phase images were both reconstructed from the data acquired with the multiecho GRE sequence by using in-house software implemented in C++ (patents have been applied for on QSM technology used in this work, and Y.W. and T.L. are listed as inventors on the applications). The entire reconstruction was fully automatic, without any user intervention to eliminate operator bias. In particular, GRE phase images were generated with the high-pass filtering method (19) by using a single echo at an echo time of 25.8 msec with a filter kernel size of 64. QSM images were automatically generated without any user intervention by using the morphology-enabled dipole inversion method (15,16,20), which took about 10 minutes to reconstruct for each patient on a personal computer equipped with a 2.4-GHz processer (Intel Core i7; Intel, Santa Clara, Calif) and 8-GB memory.

CT was performed with a 16-detector CT scanner (Lightspeed VCT; GE Healthcare, Milwaukee, Wis) with the following parameters: 250 mAs, 120 kV, 5-mm-thick sections, pitch of 1.375:1, and 512 × 512 matrix. Data were reconstructed to a 2.5-mm section thickness.

Standard of Reference

Two radiologists (W.C. [reader 1] and W.Z. [reader 2], with 10 and 21 years of experience in neuroradiology, respectively) reviewed all images obtained with both MR imaging and CT. The classification of lesions as a calcification or hemorrhage was based on the evaluation of the CT scans, conventional MR images (including T1-weighted, T2-weighted, and T2*-weighted images), and clinical information, which included medical history (eg, onset of stroke and epilepsy) and results of pathology and laboratory examinations (eg, enzyme-linked immunosorbent assay, hormone and serum electrolytes test). Intracranial lesions were identified according to the criteria listed in Table 1 and on agreement between the two readers. Each lesion was assessed according to its location, cause, and perceived susceptibility on QSM and GRE phase images (window level = 0 parts per billion). Specifically, lesions with a positive value (hyperintense) on QSM images and a negative value (hypointense) on GRE phase images were interpreted as paramagnetic. Lesions with a negative value (hypointense) on QSM images and a positive value (hyperintense) on GRE phase images were interpreted as diamagnetic (8,9,11). With incorporation of spatial features, images were characterized as homogeneously paramagnetic, homogeneously diamagnetic, primarily paramagnetic (ie, paramagnetic lesion with a small amount of diamagnetic substance), primarily diamagnetic (ie, diamagnetic lesion with a small amount of paramagnetic substance), heterogeneous (ie, lesion with approximately equal diamagnetic and paramagnetic representation), or with no conspicuous magnetic feature.

Diagnostic Accuracy Analysis

The GRE phase and QSM images were evaluated in two separate reading sessions (sessions A and B, respectively) independently by two additional radiologists (I.K. [reader 3] and A.K. [reader 4], both with more than 20

years of experience in neuroradiology) who were blinded to the patients' clinical information and the findings from the standard of reference. The session order was opposite for the two readers (session A was first for I.K. and session B was first for A.K.), and the subject order was randomized within each session. To prevent recall bias, the interval between the two sessions was at least 4 weeks (4 weeks for I.K. and 5 weeks for A.K.).

The readers were asked to categorize the individual lesions on the basis of perceived susceptibilities. Because calcifications in cortical bone, choroid plexus, and lesions are diamagnetic, whereas hemorrhages are paramagnetic (3,10,11,13,15), all paramagnetic lesions were classified as hemorrhages and diamagnetic lesions were classified as calcifications. Lesions with varying signals were classified according to their dominant signal (>70% in space). Any lesion that did not meet the diagnosis criteria listed in Table 1 or that had both calcification and hemorrhage was excluded to avoid ambiguity.

Quantitative Image Analysis

Quantitative analysis was performed on CT and MR images. Hemorrhagic lesions were excluded because their attenuations vary with age and CT is insensitive to chronic hemorrhages and microbleeds. Calcifications together with hemorrhages or inside deep brain nuclei region were excluded to avoid the confounding contributions from iron deposition. The calcified lesions detectable on both QSM and GRE phase images were included. One radiologist (W.C.) manually defined three-dimensional regions of interest by compounding two-dimensional lesion boundaries drawn on consecutive sections. Total susceptibility, total phase value (adjusted to $0–2\pi$ in each voxel), and total CT number were computed for each region of interest by summing voxel values multiplied by voxel size over the lesion volume. Then, the total susceptibility, total phase value, and total CT number for each patient were obtained by summing over all regions of interest in the patient to investigate the correlation between these quantities. Theoretically, all of these values are correlated with the total amount of deposited calcium. The lesion volumes were also calculated and compared.

Statistical Analysis

Sensitivities and specificities of using perceived susceptibility on GRE phase and QSM images to identify hemorrhages and calcifications were computed by using estimation methods for clustered binary data (21) and compared by using the Obuchowski adjustment to the McNemar test for clustered data (22–24). Interobserver agreement was assessed by calculating the Cohen κ coefficient. Linear regression was applied to determine the relationship between total CT numbers and either total susceptibility or total phase values of each patient's calcified regions, and significance was assessed with the F test. Log transformation was applied to total CT numbers, total susceptibilities, and total phase values to obtain normality for linear regression. The paired t test was used to assess the significance of difference in volume measurement among CT, GRE phase imaging, and QSM. These statistical analyses were performed with SPSS for Windows (version 16.0; SPSS, Chicago, Ill) and SAS for Windows (version 9.3; SAS, Cary, NC). $P < .05$ was considered indicative of a statistically significant difference.

Results

Appearance of Hemorrhage and Calcification at QSM and GRE Phase Imaging

A total of 156 intracranial lesions were identified with the standard of reference, of which 62 were hemorrhages, 89 were calcifications, and five were both hemorrhages and calcifications. Table 2 summarizes these lesions' magnetic characterizations, locations, and causes. Of 62 hemorrhages, 51 (82%) appeared homogeneously paramagnetic on QSM images (Fig 1c), whereas the remaining 11 (18%) appeared primarily paramagnetic with a diamagnetic surrounding rim. On GRE phase images, 31 of the 62 hemorrhages (50%) appeared heterogeneous (Fig 1d), whereas 23 (37%) appeared paramagnetic and eight (13%) appeared primarily paramagnetic.

The appearance of calcifications on QSM and GRE phase images was dependent on their locations and causes. Of the 70 calcifications outside deep brain nuclei region, QSM showed 60 lesions (86%) as homogeneously diamagnetic (Fig 1c), five (7.1%) as primarily diamagnetic with a paramagnetic surrounding rim, and five (7.1%) with no obvious magnetic signs; GRE phase imaging showed 32 of the 70 lesions (46%) as homogeneously or primarily diamagnetic, 32 (46%) as heterogeneous (Fig 1d), and six (8.6%) with no obvious magnetic signs. Of the 19 calcifications inside deep brain nuclei region that had strong paramagnetic backgrounds, QSM showed 16 (84%) as homogeneously or primarily paramagnetic (Fig 2c) and the remaining three (16%) as diamagnetic (Fig 3c); GRE phase imaging showed 13 (68%) as heterogeneous (Fig 2d), two (10%) as diamagnetic (Fig 3d), and four (21%) as paramagnetic. It was also noted that calcifications in metabolic and inflammatory diseases showed apparent paramagnetism inside the deep brain nuclei region but consistent diamagnetism outside the deep brain nuclei region (Fig E1 [online]).

When hemorrhagic and calcified lesions were combined (Table 2), QSM showed most of these lesions (146 of 151 lesions, 96.7%) distinctly as homogeneously (124 of 151 lesions, 82.1%) or primarily (22 of 151 lesions, 14.6%) paramagnetic or diamagnetic; GRE phase imaging showed about half of the lesions (76 of 151 lesions, 50.3%) as heterogeneous, making it difficult to decide whether they were diamagnetic or paramagnetic. There were five lesions with both calcifications and hemorrhage (Table 2). Although all five lesions appeared heterogeneous on

Table 2

Appearances of Hemorrhages and Calcifications at QSM and GRE Phase Imaging

Appearance	Hemorrhage ($n = 62$)	Calcifications ($n = 89$)*			Calcifications and Hemorrhages ($n = 5$)
		Congenital/Vascular/ Infections/Tumor	Inflammatory	Metabolic	
QSM					
Outside deep brain nuclei					
Diamagnetic	0	40	16	4	0
Paramagnetic	50	0	0	0	2
Primarily paramagnetic	10	0	0	0	3
Primarily diamagnetic	0	5	0	0	0
Heterogeneous	0	0	0	0	0
No conspicuous magnetic feature	0	5	0	0	0
Inside deep brain nuclei					
Diamagnetic	0	3	0	0	0
Paramagnetic	1	0	2	8	0
Primarily paramagnetic	1	0	2	4	0
Primarily diamagnetic	0	0	0	0	0
Heterogeneous	0	0	0	0	0
No conspicuous magnetic feature	0	0	0	0	0
GRE phase imaging	0				
Outside deep brain nuclei					
Diamagnetic	0	18	7	1	0
Paramagnetic	23	0	0	0	0
Primarily paramagnetic	8	0	0	0	0
Primarily diamagnetic	0	6	0	0	0
Heterogeneous	29	21	9	2	5
No conspicuous magnetic feature	0	5	0	1	0
Inside deep brain nuclei					
Diamagnetic	0	2	0	0	0
Paramagnetic	0	0	2	2	0
Primarily paramagnetic	0	0	0	0	0
Primarily diamagnetic	0	0	0	0	0
Heterogeneous	2	1	2	10	0
No conspicuous magnetic feature	0	0	0	0	0

Note.—Data are numbers of lesions.

* The causes of calcified lesions were classified according to reference 2.

GRE phase images (Fig 4d), three had dense calcified regions that could be differentiated from the paramagnetic hemorrhagic background on QSM images (Fig 4c).

Diagnostic Accuracy Analysis

Of the 156 intracranial lesions identified with the standard of reference, the five lesions with both calcifications and hemorrhages were excluded from analysis owing to the small sample size. The remaining 151 lesions with calcifications or hemorrhages were included in the diagnostic accuracy analysis. Table 3 summarizes the sensitivity and specificity of using perceived susceptibility on GRE phase and QSM images for lesion identification. Averaged over the two independent observers for detecting hemorrhages, QSM achieved a sensitivity of 89.5% and a specificity of 94.5%, which were significantly higher than those for GRE phase imaging (71% and 80%, respectively; $P < .05$ for both readers). In the identification of calcifications, QSM achieved a sensitivity of 80.5%, which is marginally higher than that for GRE phase imaging (71%; $P = .08$ and .10 for the two readers), and a specificity of 93.5%, which is significantly higher than that for GRE phase imaging (76.5%; $P < .05$ for both readers). In the differentiation of hemorrhages from calcifications, observer agreement was significantly better with QSM than with GRE phase imaging (κ: 0.91 vs 0.55, respectively; $P < .05$).

Quantitative Analysis

Sixty-four calcifications in 26 patients were included in the quantitative analysis. Linear regression analysis

Figure 1

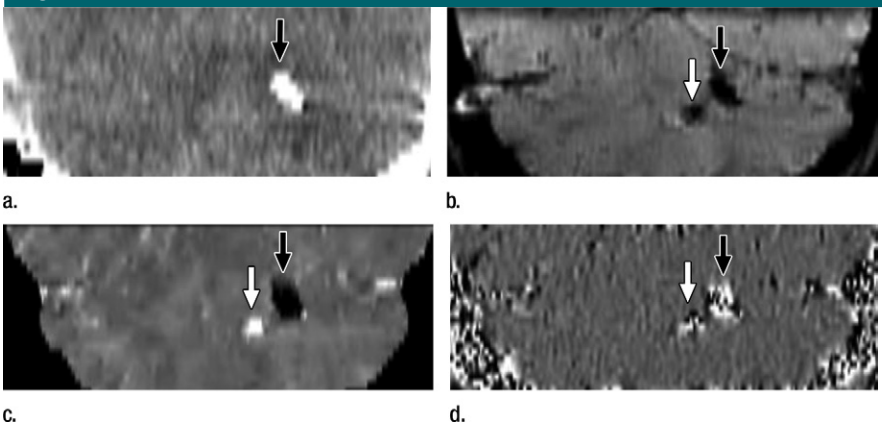

Figure 1: Calcification and hemorrhage outside deep brain nuclei in 10-year-old girl with vascular disease. Images are reformatted in coronal plane. **(a)** CT scan shows only hyperattenuating calcified lesion (arrow) (maximum CT number = 742 HU). **(b)** T2*-weighted MR image shows two hypointense lesions (arrows), one of which corresponds to calcification on **a**. **(c)** QSM image distinctly shows a diamagnetic lesion (black arrow), which corresponds to calcified lesion on **a**, and a paramagnetic lesion (hemorrhage, white arrow). **(d)** GRE phase image shows the two lesions (arrows) with heterogeneous appearances, which caused readers 3 and 4 to misclassify calcified lesion as hemorrhage.

Figure 2

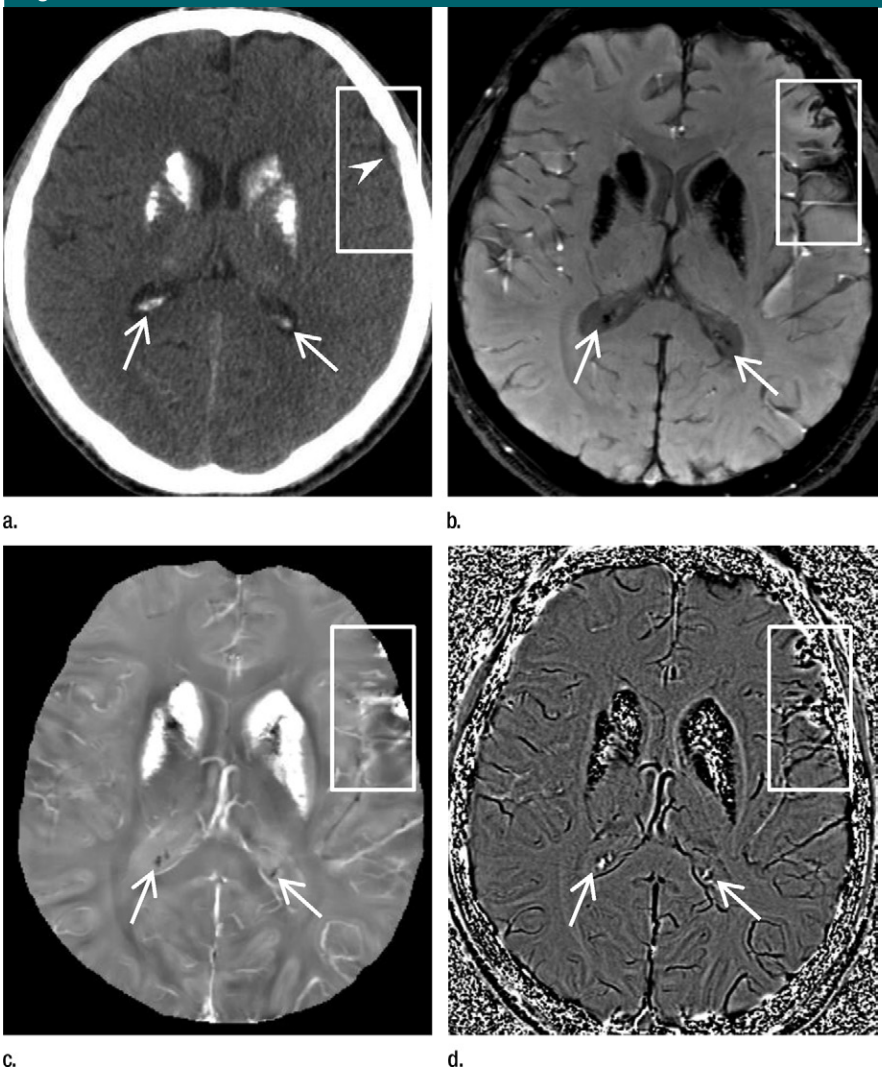

Figure 2: Calcifications (arrows) and hemorrhages (box) in 42-year-old man with hypoparathyroidism and 2-week-old traumatic brain injury. **(a)** CT scan shows hyperattenuating calcifications in bilateral basal ganglia and choroid plexus and hyperattenuating hemorrhage (arrowhead) in left frontotemporal lobe. The choroid plexus calcifications are considered physiologic. **(b)** T2*-weighted MR image shows calcifications and hemorrhages indistinctly with hypointense appearances. **(c)** QSM image shows basal ganglia as primarily paramagnetic (hyperintensity mixed with hypo- and/or isointensities), the hemorrhage as paramagnetic, and the choroid plexus calcifications as diamagnetic. **(d)** GRE phase image shows calcifications and hemorrhages indistinctly with heterogeneous appearances, causing one reader to misclassify hemorrhage as calcification.

Figure 3

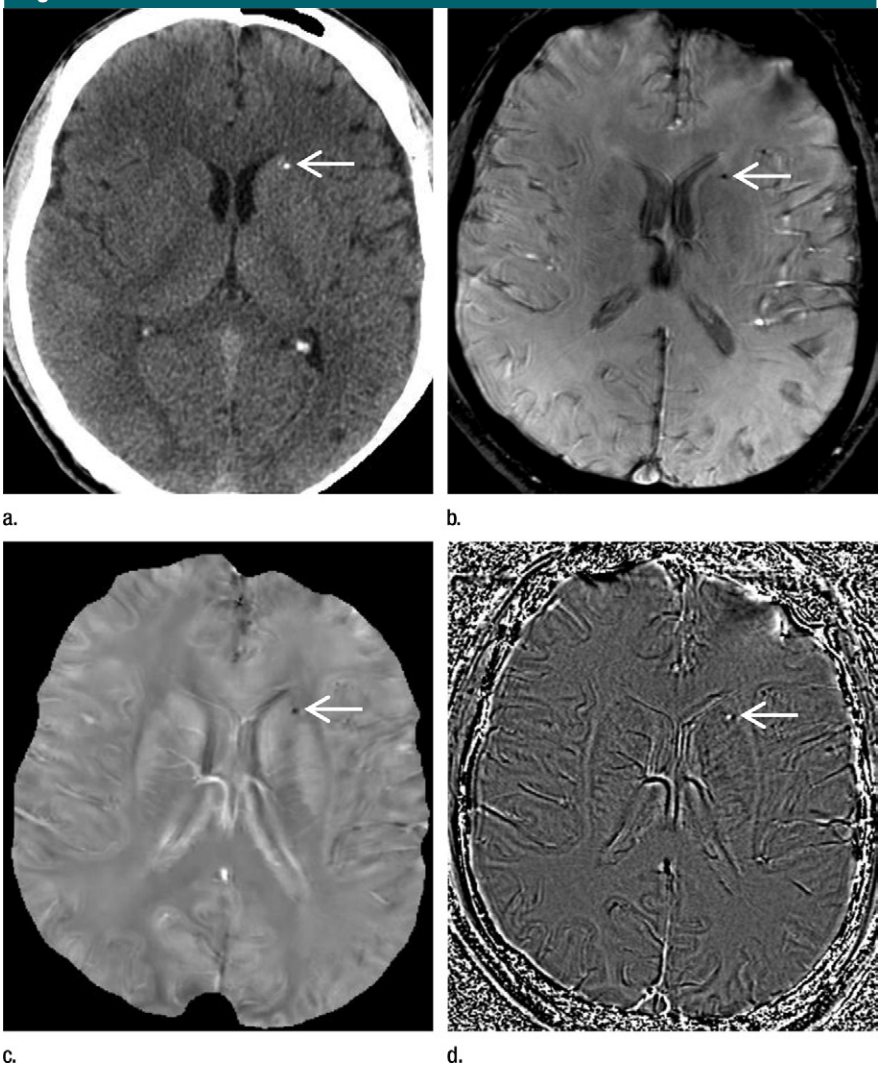

Figure 3: Calcification inside deep brain nuclei region in 26-year-old man with neurocysticercosis. A small calcified cysticercus granuloma (arrow) is seen at edge of left head of caudate nucleus and is **(a)** hyperattenuating on CT scan, **(b)** hypointense on T2*-weighted MR image, **(c)** diamagnetic on QSM image, and **(d)** diamagnetic on GRE phase image. Calcifications in choroid plexus on CT scan are absent on both QSM and GRE phase images owing to the difference in head orientations at CT and MR imaging.

showed an excellent correlation between total CT numbers and total susceptibility ($\log_{10}$ [−total susceptibility] = 0.93 × $\log_{10}$ [total CT number] + 0.22; R^2 = 0.90, $P < .001$). The correlation between total CT numbers and total phase values was instead weaker ($\log_{10}$ [total phase value] = 0.74 × $\log_{10}$ [total CT number] + 3.25; R^2 = 0.53, $P < .001$) (Fig 5).

Lesion volume measured at QSM was similar to that obtained with CT (mean volume, 0.97 cm^3 ± 4.65 and 0.99 cm^3 ± 4.7, respectively; $P = .49$). The lesion volume measured with GRE phase imaging (mean volume, 1.78 cm^3 ± 6.45) was significantly larger than that measured with QSM ($P = .015$) and CT ($P = .017$).

Discussion

Our data demonstrate that the susceptibilities of most lesions with calcification or hemorrhage are unambiguous at QSM but equivocal at GRE phase imaging, enabling better interobserver agreement with QSM than with GRE phase imaging. Further, QSM provides better sensitivity and specificity than GRE phase imaging in the detection of hemorrhages. QSM provides better specificity than GRE phase imaging in the detection of calcifications. QSM provides more accurate measurements of total susceptibility and volume for each lesion than GRE phase imaging.

GRE phase imaging has been reported to be useful for differentiating calcifications from hemorrhages (3,8,11). Recently, it has been suggested that QSM can enable the differentiation of diamagnetic calcifications from paramagnetic hemorrhages (9,17,18). To our knowledge, this study is the first systematic evaluation of the diagnostic accuracy of QSM and comparison between QSM and GRE phase imaging in the assessment of calcifications and hemorrhages. The inferiority of GRE phase imaging to QSM as found in this study may be explained as follows. First, noise may be one cause for the heterogeneous appearance on GRE phase images of lesions with poor signal-to-noise ratio, when the T2* is short for either paramagnetic (eg, hemorrhages) or diamagnetic (eg, calcifications) lesions (25). Second, the high-pass filtering used to generate GRE phase images may be a dominant cause for heterogeneity when a lesion is not small. The smooth field components (of low spatial frequencies) are removed by high-pass filtering, leaving mostly rapid spatial-varying components (of high spatial frequencies). Third, the physics underlying the phase, which reflects the magnetic field that is a nonlocal convolution of the tissue magnetic susceptibility, is a fundamental cause for the heterogeneous appearance on GRE phase images. The appearance of GRE phase images is highly dependent on imaging parameters, including field strength, echo time, voxel size, object size,

Figure 4

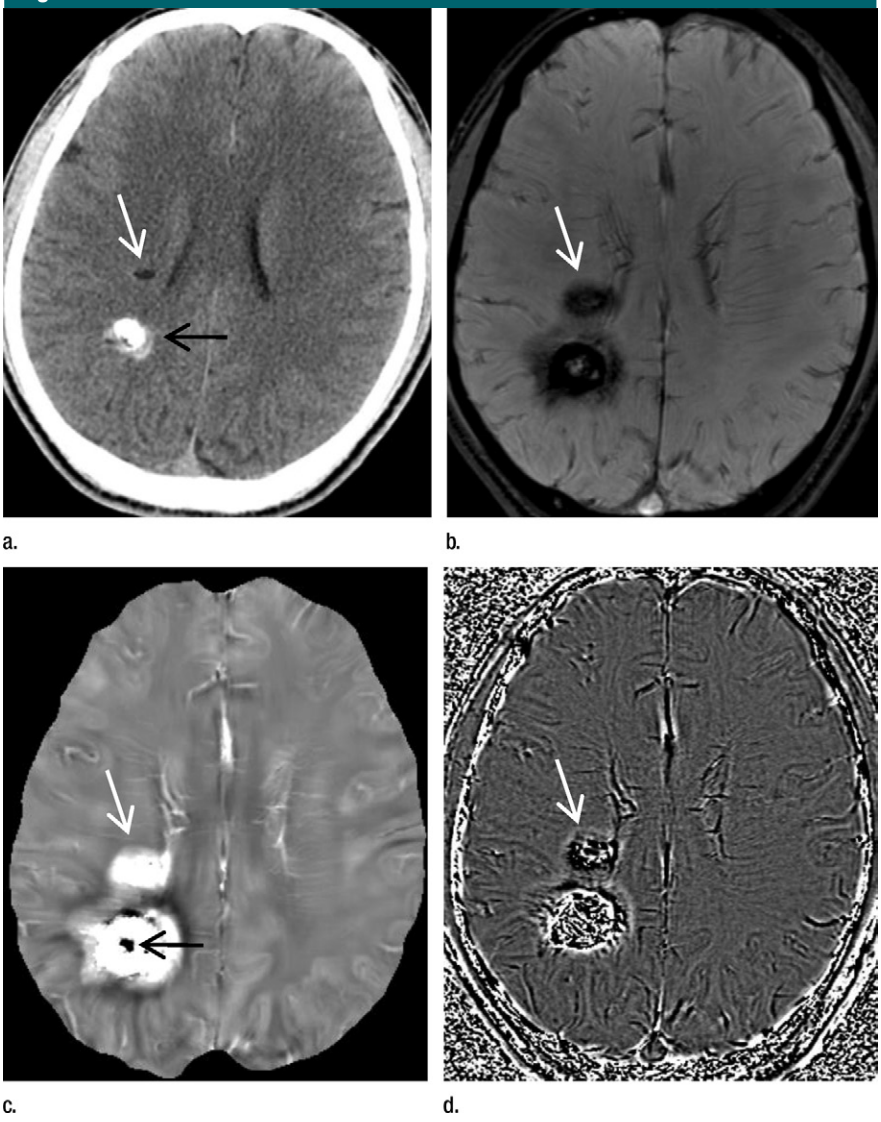

Figure 4: Calcification and hemorrhages (white arrow) in 58-year-old woman with cerebral cavernous angiomas. **(a)** CT scan shows small hypoattenuating lesion (white arrow) and hyperattenuating calcification (black arrow, CT number >200 HU). **(b)** T2-weighted MR image shows calcifications and hemorrhages indistinctly with similar appearances (hypointense lesions with iso- and/or hyperintense cores). **(c)** QSM image shows paramagnetic lesion (white arrow), which corresponds to location of small hypoattenuating lesion on CT scan and was interpreted as chronic hemorrhage, and a large primarily paramagnetic lesion mixed with a diamagnetic center (black arrow). **(d)** GRE phase image shows both lesions with heterogeneous appearances, making diagnosis difficult. Dense calcified core (black arrow in **a** and **c**) was recognized on QSM image by readers 3 and 4.

and object orientation (13,14). This may explain the discrepancies among the reported percentage of heterogeneous lesions in this study and in the literature (3,8,26). Although the total phase value showed significant correlation with the total CT number, the correlation may be mainly attributed to the size of the lesion, as the phase is almost a random variable uniformly distributed between 0 and 2π in solid calcification or hemorrhage. Therefore, when using phase information to infer tissue properties, the aforementioned confounding factors must be properly taken into account.

QSM deconvolves the nonlocal field by performing a regularized fitting process to quantitatively determine the local tissue magnetic property (13,15). The noise in the phase measurements is properly taken into account in the data weighting in the fitting according to noise probability distribution function (13). The high-pass filtering is avoided by using a background field removal technique based on the Maxwell equation (27,28). Therefore, signal in QSM directly reflects the underlying tissue susceptibility, reducing appearance ambiguity, enhancing diagnostic confidence, leading to improved sensitivity, specificity, and interobserver agreement, and providing more accurate measurements of total lesion susceptibility and volume when compared with GRE phase imaging. Our results indicate that QSM is highly accurate and can be a solution for detecting and quantifying hemorrhage and calcification lesions on MR images. It is worth reporting that QSM depicted 15 diamagnetic lesions that were invisible or slightly hyperattenuating at CT (<100 HU) in four patients with neurocysticercosis. According to the evolution of neurocysticercosis, these diamagnetic lesions might be cysticercus granuloma with low concentrations of calcium. Further pathologic or histologic validation may prove QSM to be useful in the detection of small or low calcification when the CT numbers do not reach those in the calcification diagnosis criteria.

There are limitations in the interpretation of calcification on QSM images. First, if a diamagnetic calcification is accompanied by the deposition of paramagnetic substances, such as hemosiderin in hemorrhage or ferritin in the deep brain nuclei regions, the dominant component determines the final susceptibility. As a consequence, calcifications inside the deep brain nuclei region can appear either diamagnetic or paramagnetic at QSM, which

Table 3

Diagnostic Performance of Readers 3 and 4 in the Detection of Intracranial Calcifications and Hemorrhages at QSM and GRE Phase Imaging

	QSM		GRE Phase Imaging		*P* Value	
Reader and Diagnosis	Sensitivity (%)	Specificity (%)	Sensitivity (%)	Specificity (%)	Sensitivity	Specificity
Reader 3						
Hemorrhage	90 (84, 97)	95 (89, 100)	69 (60, 79)	79 (70, 87)	.0279	.0026
Calcification	79 (63, 94)	96 (92, 100)	62 (49, 74)	80 (69, 91)	.0777	.0484
Reader 4						
Hemorrhage	89 (81, 97)	94 (89, 100)	73 (64, 81)	81 (73, 89)	.0383	.009
Calcification	82 (67, 97)	91 (85, 97)	67 (53, 82)	73 (61, 84)	.1039	.0001

Note.—Numbers in parentheses are 95% confidence intervals. QSM achieved significantly better interobserver agreements than GRE phase imaging in the differentiation of hemorrhages from calcifications (κ = 0.91 [95% confidence interval: 0.86, 0.97] and 0.55 [95% confidence interval: 0.46, 0.65], respectively).

Figure 5

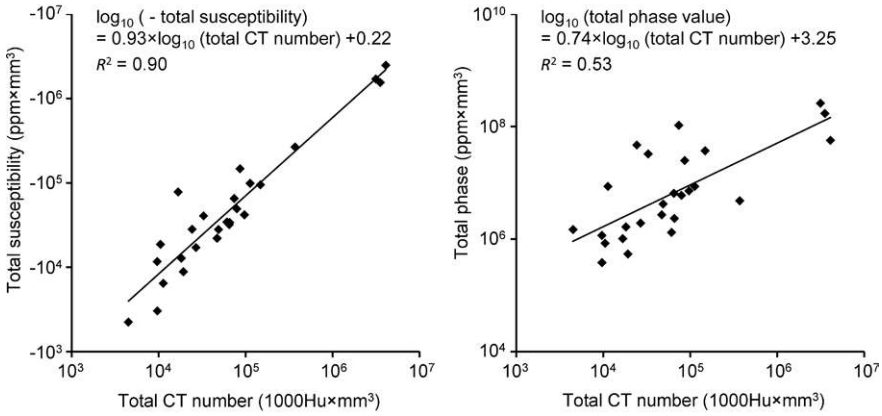

a. b.

Figure 5: Graphs show quantitative correlations between **(a)** total susceptibility versus total CT number and **(b)** total phase values versus total CT number. Total CT number shows an excellent correlation with total susceptibility (R^2 = 0.90) and a markedly lower correlation (R^2 = 0.53) with the total phase value.

is the main cause for the false-negative findings at QSM with regard to calcification detection. Second, the image quality in areas close to the skull and vessels is generally poor, possibly owing to remnant background field contribution from the air-tissue interface and phase shifts caused by blood flow. Third, there may be confounding artifacts in QSM where there is a strong susceptibility source with little detected MR imaging signal, such as in big and dense hemorrhages. The confounding artifacts in QSM generally appear as halos surrounding the source but with an opposite sign, which was the main cause of the nonuniform appearance of a same type of lesion at QSM. The current limitations call for more technical advances in QSM to further improve diagnostic accuracy.

In summary, QSM directly demonstrates the negative susceptibility of calcification and the positive susceptibility of hemorrhage and is superior to phase imaging in the specific detection of intracranial calcifications and the accurate detection of intracranial hemorrhages.

Acknowledgment: We thank Allison Dunning, MS, for statistical analyses.

Disclosures of Conflicts of Interest: W.C. No relevant conflicts of interest to disclose. **W.Z.** No relevant conflicts of interest to disclose. **I.K.** No relevant conflicts of interest to disclose. **A.K.** No relevant conflicts of interest to disclose. **T.L.** Financial activities related to the present article: none to disclose. Financial activities not related to the present article: none to disclose. Other relationships: has a patent pending with QSM Technology. **S.W.** No relevant conflicts of interest to disclose. **C.S.** No relevant conflicts of interest to disclose. **Y.W.** Financial activities related to the present article: none to disclose. Financial activities not related to the present article: none to disclose. Other relationships: has a patent pending with QSM Technology.

References

1. Huisman TA. Intracranial hemorrhage: ultrasound, CT and MRI findings. Eur Radiol 2005;15(3):434–440.
2. Makariou E, Patsalides AD. Intracranial calcifications. Appl Radiol 2009;38(11):48–60.
3. Gupta RK, Rao SB, Jain R, et al. Differentiation of calcification from chronic hemorrhage with corrected gradient echo phase imaging. J Comput Assist Tomogr 2001;25(5):698–704.
4. Kidwell CS, Chalela JA, Saver JL, et al. Comparison of MRI and CT for detection of acute intracerebral hemorrhage. JAMA 2004;292(15):1823–1830.
5. Sarmiento de la Iglesia MM, Lecumberri Cortés G, Lecumberri Cortés I, Oleaga Zufiria L, Isusi Fontan M, Grande Icaran D. Intracranial calcifications on MRI [in Spanish]. Radiologia 2006;48(1):19–26.
6. Prokop M, Galanski M. Spiral and multislice computed tomography of the body. Stuttgart, Germany: Thieme, 2003.
7. Gomori JM, Grossman RI. Mechanisms responsible for the MR appearance and evo-

lution of intracranial hemorrhage. RadioGraphics 1988;8(3):427–440.

8. Yamada N, Imakita S, Sakuma T, Takamiya M. Intracranial calcification on gradient-echo phase image: depiction of diamagnetic susceptibility. Radiology 1996;198(1):171–178.

9. Schweser F, Deistung A, Lehr BW, Reichenbach JR. Differentiation between diamagnetic and paramagnetic cerebral lesions based on magnetic susceptibility mapping. Med Phys 2010;37(10):5165–5178.

10. Wu Z, Mittal S, Kish K, Yu Y, Hu J, Haacke EM. Identification of calcification with MRI using susceptibility-weighted imaging: a case study. J Magn Reson Imaging 2009;29(1):177–182.

11. Zhu WZ, Qi JP, Zhan CJ, et al. Magnetic resonance susceptibility weighted imaging in detecting intracranial calcification and hemorrhage. Chin Med J (Engl) 2008;121(20):2021–2025.

12. Liu T, Spincemaille P, de Rochefort L, Kressler B, Wang Y. Calculation of susceptibility through multiple orientation sampling (COSMOS): a method for conditioning the inverse problem from measured magnetic field map to susceptibility source image in MRI. Magn Reson Med 2009;61(1):196–204.

13. de Rochefort L, Liu T, Kressler B, et al. Quantitative susceptibility map reconstruction from MR phase data using bayesian regularization: validation and application to brain imaging. Magn Reson Med 2010;63(1):194–206.

14. Li J, Chang S, Liu T, et al. Reducing the object orientation dependence of susceptibility effects in gradient echo MRI through quantitative susceptibility mapping. Magn Reson Med 2012;68(5):1563–1569.

15. Liu J, Liu T, de Rochefort L, et al. Morphology enabled dipole inversion for quantitative susceptibility mapping using structural consistency between the magnitude image and the susceptibility map. Neuroimage 2012;59(3):2560–2568.

16. Liu T, Wisnieff C, Lou M, Chen W, Spincemaille P, Wang Y. Nonlinear formulation of the magnetic field to source relationship for robust quantitative susceptibility mapping. Magn Reson Med 2013;69(2):467–476.

17. Liu T, Surapaneni K, Lou M, Cheng L, Spincemaille P, Wang Y. Cerebral microbleeds: burden assessment by using quantitative susceptibility mapping. Radiology 2012;262(1):269–278.

18. Deistung A, Schweser F, Wiestler B, et al. Quantitative susceptibility mapping differentiates between blood depositions and calcifications in patients with glioblastoma. PLoS ONE 2013;8(3):e57924.

19. Wang Y, Yu Y, Li D, et al. Artery and vein separation using susceptibility-dependent phase in contrast-enhanced MRA. J Magn Reson Imaging 2000;12(5):661–670.

20. Liu T, Liu J, de Rochefort L, et al. Morphology enabled dipole inversion (MEDI) from a single-angle acquisition: comparison with COSMOS in human brain imaging. Magn Reson Med 2011;66(3):777–783.

21. McCarthy WF, Guo N. The estimation of sensitivity and specificity of clustered binary data. In: Proceedings of the 31st Annual SAS Users Group International Conference. Cary, NC: SAS Institute 2006; 1–6.

22. Lieber ML, Ashley C. A SAS macro implementing an extension of McNemar's test for clustered data. In: Proceedings of the 23rd Annual SAS Users Group International Conference. Cary, NC: SAS Institute 1998; 1–6.

23. Obuchowski NA. On the comparison of correlated proportions for clustered data. Stat Med 1998;17(13):1495–1507.

24. Trajman A, Luiz RR. McNemar χ^2 test revisited: comparing sensitivity and specificity of diagnostic examinations. Scand J Clin Lab Invest 2008;68(1):77–80.

25. Conturo TE, Smith GD. Signal-to-noise in phase angle reconstruction: dynamic range extension using phase reference offsets. Magn Reson Med 1990;15(3):420–437.

26. Gronemeyer SA, Langston JW, Hanna SL, Langston JW Jr. MR imaging detection of calcified intracranial lesions and differentiation from iron-laden lesions. J Magn Reson Imaging 1992;2(3):271–276.

27. Liu T, Khalidov I, de Rochefort L, et al. A novel background field removal method for MRI using projection onto dipole fields (PDF). NMR Biomed 2011;24(9):1129–1136.

28. Schweser F, Lehr BW, Deistung A, Reichenbach JR. A novel approach for separation of background phase in SWI phase data utilizing the harmonic function mean value property [abstr]. In: Proceedings of the Eighteenth Meeting of the International Society for Magnetic Resonance in Medicine. Berkeley, Calif: International Society for Magnetic Resonance in Medicine, 2010; 142.